3-D Discrete Analytical Ridgelet Transform

David Helbert, Philippe Carré, Éric Andrès

HAL Id: hal-00331384
https://hal.science/hal-00331384

Submitted on 16 Oct 2008

3-D Discrete Analytical Ridgelet Transform

David Helbert, Philippe Carré, and Eric Andres,

Abstract

In this paper, we propose an implementation of the 3-D ridgelet transform: The 3-D Discrete Analytical Ridgelet Transform (3-D DART). This transform uses the Fourier strategy for the computation of the associated 3-D discrete Radon transform. The innovative step is the definition of a discrete 3-D transform with the discrete analytical geometry theory by the construction of 3-D discrete analytical lines in the Fourier domain. We propose two types of 3-D discrete lines: 3-D discrete radial lines going through the origin defined from their orthogonal projections and 3-D planes covered with 2-D discrete line segments. These discrete analytical lines have a parameter called arithmetical thickness, allowing us to define a 3-D DART adapted to a specific application. Indeed, the 3-D DART representation is not orthogonal, It is associated with a flexible redundancy factor.

The 3-D DART has a very simple forward/inverse algorithm that provides an exact reconstruction without any iterative method. In order to illustrate the potentiality of this new discrete transform, we apply the 3-D DART and its extension to the Local-DART (with smooth windowing) to the denoising of 3-D image and colour video. These experimental results show that the simple thresholding of the 3-D DART coefficients is efficient.

Index Terms

3-D ridgelet transform, discrete analytical objects, denoising, video, colour images

I. INTRODUCTION

A team from University of Stanford has recently developed an alternative system of multiresolution analysis, called ridgelet transform, specifically designed to efficiently represent edges in images [1]. The ridgelet transform can be computed by performing a wavelet analysis in the Radon domain. However, most of the work done with ridgelets has been theoretical in nature. To our knowledge, we can only find in literature three main implementations for the 2-D discrete ridgelet decomposition [2]–[4]. This paper presents an extension to 3-D of our approach proposed in [4] that aims at representing linear singularities with a discrete ridgelet transform based on discrete analytical objects: the 3-D Discrete Analytical ridgelet Transform (3-D DART). The idea behind the 3-D associated discrete Radon transform is to define each Radon projection by a 3-D discrete analytical line in the Fourier domain. There are several advantages in using discrete analytical lines:

- They offer a theoretical framework for the definition of the 3-D discrete Radon projections.
- This solution allows us to have different ridgelet decompositions according to the arithmetical thickness of the 3-D discrete lines (control of the representation redundancy factor).
- The 3-D DART has a very simple forward/inverse algorithm (It is an important quality for the 3-D computation).
- The simple straightforward approach ensures an exact reconstruction without any interpolation or iterative process.

In section II, we will present the ridgelet transform. In section III, we will define the 3-D discrete analytical Radon transform with two geometrical approaches. In section IV, we will present the 3-D Discrete Analytical ridgelet Transform. In order to illustrate the performances of the 3-D DART, we have applied our transform and its local extension to the denoising of some 3-D images in section V and colour videos in section VI.

II. THE RIDGELET TRANSFORM

A. The Continuous Ridgelet Transform

The 2-D continuous ridgelet theory is documented in the Ph.D. thesis of Candès [1]. The ridgelet transform of $f \in L^2 \left(\mathbb{R}^3 \right)$[1] is extended to 3-D case by [5]–[7]:

$$r \left(a, b, \theta, \gamma \right) = \int_{\mathbb{R}^3} \overline{\psi}_{a,b,\theta,\gamma} \left(\mathbf{x} \right) f \left(\mathbf{x} \right) d\mathbf{x} \tag{1}$$

with $\mathbf{x} = (x_1, x_2, x_3)$.

[1]$f \in L^2 \left(\mathbb{R}^3 \right)$ if $\int_{\mathbb{R}^3} \| f(x_1, x_2, x_3) \|^2 dx_1 dx_2 dx_3 < \infty$

The ridgelet 3-D function $\psi_{a,b,\theta,\gamma}$ is defined from a wavelet 1-D function ψ, $b \in \mathbb{R}$ is the translation parameter, $a \in \mathbb{R}^{*+}$ is the dilatation parameter and $\theta \in [0, 2\pi[$, $\gamma \in [0, \pi[$ are the direction parameters:

$$\psi_{a,b,\theta,\gamma} : \mathbb{R}^3 \to \mathbb{R} \tag{2}$$

$$\psi_{a,b,\theta,\gamma}(x_1, x_2, x_3) = \tag{3}$$

$$\psi\left(\frac{x_1 \cos\theta \cos\gamma + x_2 \sin\theta \cos\gamma + x_3 \sin\gamma - b}{a}\right) \tag{4}$$

The function $\psi_{a,b,\theta,\gamma}$ is oriented at the angles θ and γ and is constant along lines:

$$x_1 \cos\theta \cos\gamma + x_2 \cos\theta \sin\gamma + x_3 \sin\theta = cst. \tag{5}$$

As for the 2-D case, a basic tool to calculate ridgelet coefficients is to view the ridgelet analysis as a wavelet analysis in the Radon domain. The 3-D Radon transform of f noted R_f is defined as:

$$R_f(t, \theta, \gamma) = \int_{\mathbb{R}^3} f(\mathbf{x})$$
$$\delta(x_1 \cos\theta \cos\gamma + x_2 \cos\theta \sin\gamma + x_3 \sin\theta - t) \, d\mathbf{x} \tag{6}$$

with δ is Dirac's delta function defined by:

$$\delta(x) = 0 \quad \forall x \neq 0 \tag{7}$$

$$\int_{-\infty}^{\infty} \delta(x) = 1 \tag{8}$$

The ridgelet coefficients r_f of f are given by the 1-D wavelet transforms on projections of the Radon transform R_f where the directions θ, γ are constant and t is varying:

$$r(a, b, \theta, \gamma) = \int_{\mathbb{R}} \psi_{a,b}(t) R_f(t, \theta, \gamma) \, dt \tag{9}$$

The 3-D continuous Radon transform can be defined using 1-D projections of a 3-D object f where these projections are obtained by integrating f on a plane [8]. The 3-D continuous Radon transform of an object is related to its 3-D Fourier transform via the central slice theorem:

$$R_f(t, \theta, \gamma) = \int_{\mathbb{R}} \widehat{f}(\xi \cos\theta \cos\gamma, \xi \cos\theta \sin\gamma, \xi \sin\theta) e^{j\xi t} d\xi \tag{10}$$

with $\widehat{f}$ the 3-D Fourier transform of f.

B. The Discrete ridgelet transform

As we have seen, a basic strategy to calculate the continuous ridgelet transform is first to compute the Radon transform R_f and secondly, to apply a 1-D wavelet transform to the slices $R_f(., \theta, \gamma)$. The discrete procedure uses the same principle.

The discrete wavelet decomposition is easy to implement and, when associated with a filter bank [9], is stable and invertible. It can be associated with a discrete orthogonal representation.

The discretization of the Radon transform is more difficult to achieve. The majority of methods proposed in literature, for the 2-D case, have been devised for computerized tomography or to approximate to the continuous formula [10]–[18]. But, none of them were specifically designed to be invertible transforms for discrete images and cannot be used for the discrete ridgelet transform. Some articles have recently studied the implementation of the digital 2-D ridgelet transform using two different approaches to compute the discrete Radon transform: the spatial strategy (summations of image pixels over a certain set of lines) and the Fourier strategy.

Do and Vetterli proposed in [19], [20] an orthonormal ridgelet transform with the implementation of the finite Radon transform. This Radon transform integrates over lines (that are defined algebraically rather than geometrically) with points that can be rather arbitrarily spread out over the spatial domain. The finite ridgelet transform is not redundant [2] but has constraints on the size of images.

The Fourier strategy for digital Radon transform is based on the projection-slice formula suggesting that approximate Radon transforms for digital data can be based on Discrete Fourier transforms. This is a widely used approach in the literature of medical imaging and synthetic aperture radar imaging. In this strategy too, discrete lines must be defined. The two Stanford's university algorithms [21], [22] consist in substituting the sampled value of the Fourier transform obtained on the square lattice with sampled value of $\widehat{s}$ on a polar lattice. In [21], Averbuch et Al proposed the Fast Slant Stack based on a chirp-Z transform which requires an iterative approximation algorithm for the inverse transform. In [22], Starck et al proposed to use a simple nearest-neighbor interpolation scheme.

---

[2]Redundancy of the transform is defined by: $\rho = \frac{\text{number of transform coefficients}}{\text{number of image pixels}}$

In [23] and [4], Carré and Andres proposed to define the discrete lines with discrete analytical geometry in the 2-D Fourier domain. This solution allows them to have different ridgelet decompositions according to the arithmetical thickness of the discrete lines. The transformation is redundant but the repetition of information depends on the type of the discrete lines used and can be adapted to the application. Moreover this method is associated with a non-iterative inverse algorithm that gives an exact reconstruction. In this paper, we present the extension of the 2-D discrete strategy to the 3-D space to define a reversible 3-D discrete ridgelet transform. Preliminar results of this study are presented in [24], [25].

In the literature, some 3-D discrete Ridgelet transforms, or associated representations such as Curvelet and Beamlet, have been recently proposed:

- Querre, Starck, Donoho et al. proposed an extension of their 2-D strategy [5]–[7]. In the Fourier domain, a cartesian-to-spherical conversion is used: they define for this an interpolation scheme that substitute the sampled values on the cartesian system with sampled values in a spherical system. Since the aim of these papers is to develop tools for analysis of 3-D data (for example, Querre et al. have proposed a 3-D extension of discrete ridgelet transform in [5] to present a statistical tool to describe galaxy distribution) the interpolation scheme is not presented and the inversion is not discussed.
- Averbuch et al [8], [26] have recently proposed an extension of the Fast Slant Stack to the 3-D case. They use the same strategy than Starck, Donoho et al, but they define and study a very complete interpolation scheme in the Fourier domain. As for the 2-D case, they use the fractional Fourier transform and they obtained the same properties than for the 2-D transform (algebraic exactness, geometric fidelity and parallels with continuum theory). However even though the invertibility of the decomposition is shown, no reconstruction algorithm is given (it is not defined so far in 3-D).

All these decompositions are right now used for 3-D image structure analysis but not for video denoising because of the difficult inversion problem.

Other 3-D discrete multiscale transforms have been recently proposed:

- Selesnick proposed an extension to the 3-D case of the dual tree complex wavelet transform [27]. With this new decomposition, a denoising strategy is defined and applied on video. A ©Matlab toolbox for 3-D oriented transforms is available on http://taco.poly.edu/WaveletSoftware/. This 3-D oriented transform isolates motion in different directions in separate subbands and can also represent motion information.
- Ying et al. have proposed very recently a 3-D discrete Curvelet transform [28]. Contrary to the previous implementations of Curvelet that used the Ridgelet transform [22], they propose two direct implementations based on localizing windows in the Fourier domain. The first strategy uses the unequispaced FFT (with an interpolation process) and requires an iterative reconstruction algorithm. The second implementation is based on the wrapping of Fourier samples. In this case, the inverse transform is computed as the adjoint of the forward transform.
- Lu and Do proposed a family of filter banks, named 3-D directional filter banks [29], that decomposes a 3-D signal into directional subbands with a tree structured construction. They also proposed an multiresolution transform, named the surfacelet transform, by combining the 3-D directional filter banks with the Laplacian pyramid.

In this paper, the 3-D dual tree complex wavelet transform and the 3-D undecimated wavelet transform are used as a reference 3-D transform to compare denoising results with the 3-D DART in section VI.

III. THE 3-D DISCRETE ANALYTICAL RADON TRANSFORM

A. Principles of the 3-D Discrete Radon Transform

The discretization of the 3-D Radon transform is the extension of the 2-D discrete Radon transform method:

1) Compute the 3-D Discrete Fourier Transform of f,
2) Extract Fourier coefficients that belong to straight lines $L_{\theta,\gamma}$ going through the origin,
3) Compute the 1-D Discrete Fourier Transform on each line $L_{\theta,\gamma}$ (defined for each value of the two angular parameters).

The idea (as proposed in [4], [23] in 2-D case) is to represent each direction with an analytical 3-D discrete straight line in the Fourier domain.

For the 3-D discrete Radon transform, we need a discrete 3-D straight line that has a central symmetry and forms a "good" approximation of the corresponding Euclidian straight line (i.e. direction). Moreover, if our transform is to be perfectly invertible, the discrete 3-D straight lines need to cover all the Fourier domain (each point of the Fourier domain belongs to at least one discrete 3-D line).

Since none of the "classical" notions of discrete 3-D lines fits all of these conditions, we propose our own families of discrete 3-D lines with help of the discrete analytical geometry. An important body of theory is available in [30], [31].

We propose two methods to define 3-D discrete lines covering all 3-D cubic lattice:

1) Cover the 3-D cubic lattice with 3-D discrete radial lines going through the origin defined from their orthogonal projections [25].

2) Cover the 3-D cubic lattice with a specific set of 3-D planes [24]. Each discrete plane is then being covered with a set of 2-D line segments.

In order to explain these two constructions, we first propose to review briefly the principle of 2-D discrete analytical lines.

B. 2-D Discrete Lines

The 2-D discrete lines that are used in the DART application are not classical discrete lines (which do not provide a central symmetry in the Fourier domain). Central symmetry is easily obtained by defining an analytical discrete lines from the cartesian point $O(0,0)$ to the cartesian point $P(p,q)$ [30]:

$$L^{\omega_L}_{(p,q)} = \left\{ (x,y) \in \mathbb{Z}^2 \,\middle|\, |qx - py| \leq \frac{\omega_L}{2} \right\} \tag{11}$$

with $(p,q) \in \mathbb{Z}^2$ the direction of the line and ω_L, function of p and q, is called the arithmetical thickness. It allows us to control the redundancy of the transform and the topological properties of the discrete analytical lines (the discrete line connexity). For example, if $\omega_L < \max(|p|, |q|)$, the discrete line is not connected. Three different types of closed discrete lines have been tested:

- closed naive discrete lines: $\omega_L = \max(|p|, |q|)$. These lines (figure 1(a)) are the thinnest connected closed discrete lines. They are 8-connected [3]
- closed Pythagorician lines: $\omega_L = \sqrt{p^2 + q^2}$. These lines (figure 1(b)) are 8-connected and offer a medium redundancy, between the naive and supercover lines.
- supercover lines: $\omega_L = |p| + |q|$. These lines (figure 1(c)) are the thickest connected closed discrete lines that have been considered in our applications [31]. They are the thinnest closed lines that are 4-connected and that cover the Euclidean line they approximate.
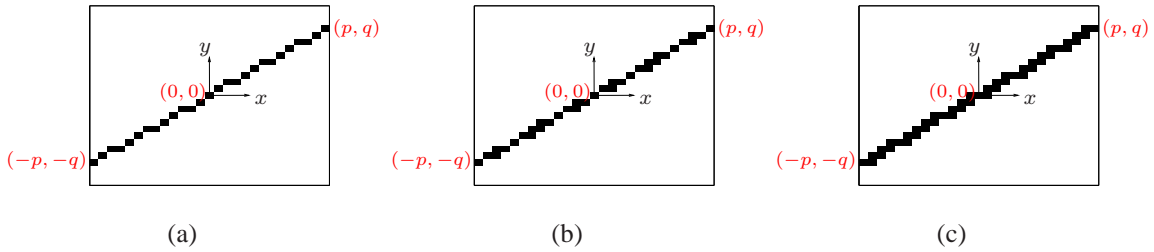

Fig. 1. The analytical 2-D discrete lines: (a) closed naive ($\omega_L = \max(|p|, |q|)$), (b) closed pythagorician ($\omega_L = \sqrt{p^2 + q^2}$) and (c) supercover ($\omega_L = |p| + |q|$).

C. Definition of 3-D Supercover Lines

First we propose to cover the 3-D cubic lattice with 3-D discrete lines.

The supercover 3-D straight line is defined by the intersection of the extrusion of three orthogonal projections (figure 2). In the cartesian domain, the supercover 3-D discrete line $L^{\omega_1, \omega_2, \omega_3}_{(p,q,r)}$ linking the cartesian points $O(0,0,0)$ and $Q(p,q,r)$ is defined by:

$$L^{\omega_1, \omega_2, \omega_3}_{(p,q,r)} = \pi_{oxy}(p,q,r) \cap \pi_{oyz}(p,q,r) \cap \pi_{ozx}(p,q,r) \tag{12}$$

with:

$$\pi_{oxy}(p,q,r) = \left\{ (x,y,z) \in \mathbb{Z}^3 \mid |qx - py| \leq \frac{\omega_1}{2} \right\} \tag{13}$$

$$\pi_{oyz}(p,q,r) = \left\{ (x,y,z) \in \mathbb{Z}^3 \mid |ry - qz| \leq \frac{\omega_2}{2} \right\} \tag{14}$$

$$\pi_{ozx}(p,q,r) = \left\{ (x,y,z) \in \mathbb{Z}^3 \mid |pz - rx| \leq \frac{\omega_3}{2} \right\} \tag{15}$$

$qx - py = 0$ is the 2-D discrete line equation linking $(0,0)$ and (p,q), result from the orthogonal projection of OQ on the plane Oxy. The analytical 3-D discrete line arithmetical thickness in the direction Ox, Oy and Oz is represented by $\omega_1 = |p| + |q|$, $\omega_2 = |q| + |r|$ and $\omega_3 = |r| + |p|$. $(p,q,r) \in \mathbb{Z}^3$ is the direction of the line (and corresponds to the (θ, γ) direction of Radon projection of equation 6).

---

[3]Two pixels $P(x_p, y_p)$ and $Q(x_q, y_q)$ are 4-connected if and only if $|x_p - x_q| + |y_p - y_q| \leq 1$. P and Q are 8-connected if and only if $\max(|x_p - x_q|, |y_p - y_q|) \leq 1$.
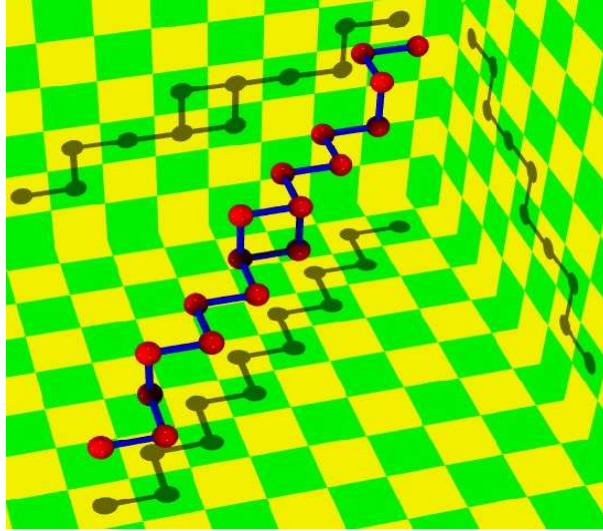
Fig. 2. A 3-D supercover line with this three orthogonal projections [31].

At last, the set of discrete directions (p, q, r) for a complete representation has to be determined. The set of line segments must cover all the cubic lattice in the Fourier domain. For this, in the 2-D case we define the directions according to pairs of symmetric points from the boundary of the 2-D discrete Fourier spectra. We know from [23] (this result is reviewed at appendix I) that if a discrete line $L_{(p,q)}^{\omega_L}$ satisfies $\omega_L \geq \max(|p|, |q|)$ then the set of all discrete analytical lines provides a complete cover of the lattice.

We propose to generalize this strategy and the set of discrete directions (p, q, r) for a complete representation is determined according to pairs of central symmetric points from the boundary of the 3-D Fourier domain.

Figure 3 shows how the 3-D discrete lines that cover the 3-D Fourier domain are chosen. As this 3-D discrete analytical lines is not always connected, the 3-D Fourier spectra is not always covered.
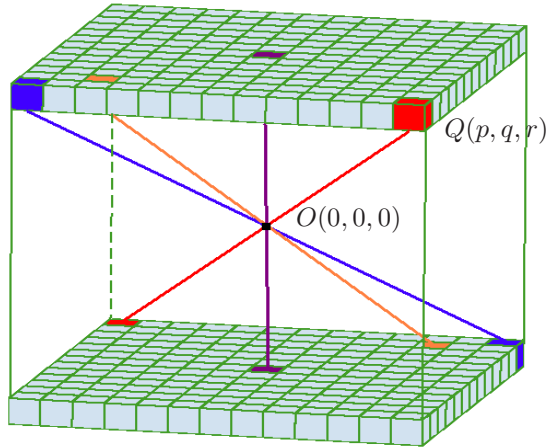

Fig. 3. Covering of the 3-D Fourier domain with 3-D discrete lines: definition of different 3-D Euclidian lines according to the central symmetry and extremity coordinates.

If $\pi_{oxy}(p, q, r)$, $\pi_{oyz}(p, q, r)$ and $\pi_{ozx}(p, q, r)$ are 2-D supercover lines, then $L_{(p,q,r)}^{\omega_1, \omega_2, \omega_3}$ is the supercover of the 3-D Euclidian line OQ (figure 4(c)), studied in discrete analytical geometry [31]. However, experience shows that if $\omega_1 < |p| + |q|$, $\omega_2 < |q| + |r|$ and $\omega_3 < |r| + |p|$, then the discrete 3-D analytical lines $L_{(p,q,r)}^{\omega_1, \omega_2, \omega_3}$ is not necessary connected (figures 4(a) and 4(b)) and thus the 3-D Fourier domain is not always entirely covered. The following proposition shows that the supercover lines always cover the cubic lattice.

Proposition 1 :
Let a cubic lattice be defined as $\Omega_N^3 = [-N, N] \times [-N, N] \times [-N, N]$.
The supercover 3-D lines $L_{(p,q,r)}^{|p|+|q|,|q|+|r|,|r|+|p|}$ provides a complete cover of the lattice Ω_N^3.

Proof :

Let's consider a point A of the cubic lattice Ω_N^3, and $O(0,0,0)$ the center of Ω_N^3. We will demonstrate that A is element of a supercover line.

Let's suppose that the line OA intersects the border of Ω_N^3 in a point $B(x_B, y_B, N)$ with $(x_B, y_B) \in R^2$ (all the others cases are symetric).

The supercover line of 3-D straight line L noted noted $\mathbb{S}(L)$ can also be defined by [32]:

$$\mathbb{S}(L) \quad = \quad \left\{ k \in \mathbb{Z}^n \left| d^\infty(k, L) \leq \frac{1}{2} \right. \right\} \tag{16}$$

$$= \quad \left(L \oplus \mathbb{B}^\infty \left(\frac{1}{2} \right) \right) \cap \mathbb{Z}^n \tag{17}$$

where $\oplus$ is the Minkowski sum, $d^\infty(x, y) = \sup_{1 \leq i \leq n} |x_i - y_i|$, $x = \{x_1, x_2, .., x_N\}$, $y = \{y_1, y_2, .., y_N\}$ and $\mathbb{B}^\infty(\frac{1}{2})$ ball of radius $\frac{1}{2}$ for the distance d^∞ (a cube of side equal to 1).

A supercover of the 3-D Euclidian line $\mathbb{S}(L)$ corresponds to the extrusion of a ball $\mathbb{B}^\infty(\frac{1}{2})$, that is to say a cube of side equal to 1, along the Euclidian line L.

There exists a point $C(x_c, y_c, N)$ with $(x_C, y_C) \in Z^2$ such that $d^\infty(B, C) \leq \frac{1}{2}$ (it is easy to see from figure 3 that this is always true for d^∞).

From there, Thales tells us that $d^\infty(A, OC) \leq \frac{1}{2}$ since $d^\infty(OB, OC) \leq \frac{1}{2}$ and thus $A \in \mathbb{S}(OC)$. $\diamond$

With the first 3-D line definition, only supercover lines cover the cubic lattice (the proposition restricts the choice of possible thickness ω_1, ω_2 and ω_3). This is why we have proposed an other method based discrete 2-D lines covering properties.
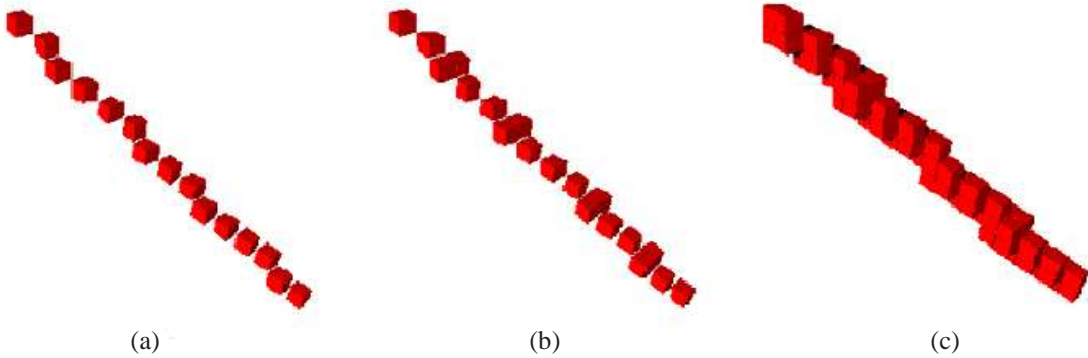

Fig. 4. 3-D discrete lines: (a) closed naive: $\omega_1 = \max(p, q)$, $\omega_2 = \max(q, r)$, $\omega_3 = \max(r, p)$, (b) closed pythagorician: $\omega_1 = \sqrt{p^2 + q^2}$, $\omega_2 = \sqrt{q^2 + r^2}$, $\omega_3 = \sqrt{r^2 + p^2}$ (c) supercover: $\omega_1 = |p| + |q|$, $\omega_2 = |q| + |r|$, $\omega_3 = |r| + |p|$.

D. Method Based on the Extrusion of Discrete 2-D Analytical Lines

This method has been first proposed in [24], [25]. The idea is to use covering properties that we have in 2-D to define discrete 3-D lines preserving these properties: cover the 3-D cubic lattice with a specific set of 3-D planes and each discrete plane is then being covered with a set of 2-D line segments.

To compute a discrete plane $P_{[r,s]}^{\omega_P}$ for our application [33], we need to define the analytical 2-D discrete line $L_{[r,s]}^{\omega_P} = \left\{ (x,y) \in \mathbb{Z}^2 \left| |rx + sy| \leq \frac{\omega_P}{2} \right. \right\}$ and the discrete plane is obtained by the extrusion of the analytical 2-D discrete line along the z-axis (the central plane axis is chosen arbitrarily).

Then, the 3-D cubic lattice is covered with discrete analytical 3-D planes defined by the following equation (figure 5):

$$P_{[r,s]}^{\omega_P} = \left\{ (x, y, z) \in \mathbb{Z}^3 \left| |sx - ry + 0 \cdot z| \leq \frac{\omega_P}{2} \right. \right\} \tag{18}$$

where $(r, s) \in \mathbb{Z}^2$ are the γ direction of the plane and ω_P, function of r and s, is the arithmetical thickness. These planes have a central symmetry and are the analytical discretization of the Euclidean planes $P_\gamma : sx - ry + 0 \cdot z = 0$ for a given arithmetical thickness w_P.

Each 2-D line gives a 1-D row and all the lines provides a 2-D domain. This construction is illustrated in figure 6. We thus extract Fourier coefficients from $P_{[r,s]}^{\omega_P}$ and we cover this 2-D domain with discrete 2-D analytical lines $L_{[p,q]}^{\omega_L} = \left\{ (u, v) \in \mathbb{Z}^2 \left| |pu + qv| \leq \frac{\omega_L}{2} \right. \right\}$ where (p, q) are the θ direction (this discrete 3-D line can be viewed as intersection of two orthogonal discrete planes). The lines are covered in a natural way as illustred in figure 6.
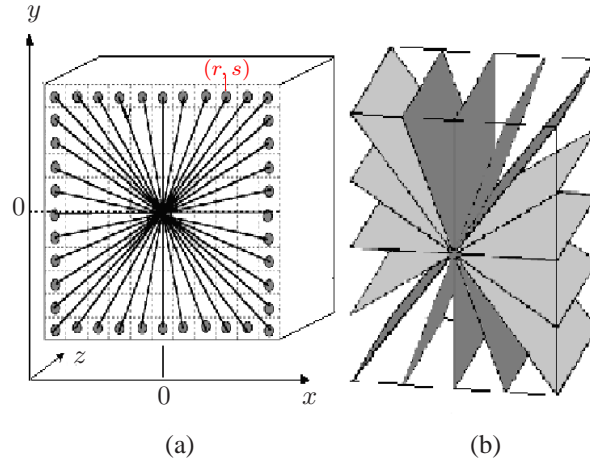
Fig. 5.   (a) Choice of the discrete discrete lines $L_{[r,s]}^{\omega_P}$, (b) cover of the 3-D Fourier domain with Euclidian planes.
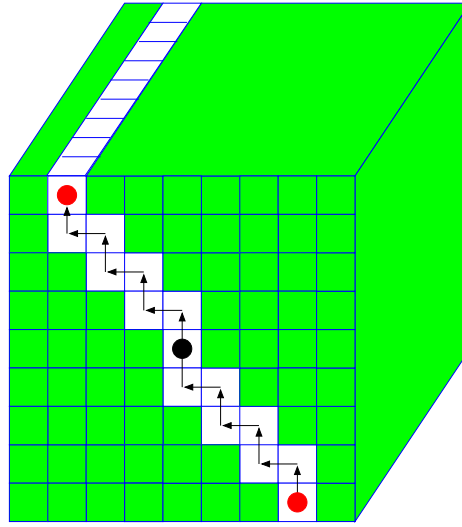

Fig. 6.   Fourier coefficients extraction along the discrete analytical line.

At last, the set of discrete directions $[p, q]$ (associated with the lines) and $[r, s]$ (associated with the planes) for a complete representation has to be determined. The set of 3-D line segments must cover all the cubic lattice in the Fourier domain. It has been shown in [4] that 2-D lines $|px + qy| \leq \frac{\omega_L}{2}$ chosen according to pairs of symmetric points from the boundary of the 2-D discrete Fourier spectra (as in figure 5(a)) cover the 2-D Fourier domain when the arithmetical thickness verifies $\omega_L \geq \max(|p|, |q|)$ (appendix I).

In order to cover all the cubic lattice in the Fourier domain, we thus define the directions according to pairs of symmetric points from the boundary of:

- the plane $\{z = 0\}$ for the planes $P_{[r,s]}^{\omega_P}$.
- the plane $P_{[r,s]}^{\omega_P}$ for the lines $L_{(p,q)}^{\omega_L}$.

According to the 2-D domain, the 3-D Fourier domain is always covered by the analytical 3-D discrete lines if $\omega_P \geq \max(|r|, |s|)$ and $\omega_L \geq \max(|p|, |q|)$.

E. Computation of the 3-D discrete analytical Radon transform

We have proposed two strategies to define 3-D discrete lines. Now, we can use the Fourier domain for the computation of our discrete Radon transform. For this, Fourier coefficients of $\widehat{f}$ are extracted along the proposed 3-D discrete analytical lines and ordered in a natural way (as illustrated in figure 6):

$$Q_{\Theta}^{\omega} = Q_{[p,q,r]}^{\omega_1, \omega_2, \omega_3} = \cup_{k \in \mathcal{Z}^+} \widehat{f} \left(\nu_1^k, \nu_2^k, \nu_3^k \right) \tag{19}$$

with $\left(\nu_1^k, \nu_2^k, \nu_3^k\right) \in L_{(p,q,r)}^{\omega_1,\omega_2,\omega_3}$ for the 3-D construction or

$$Q_\Theta^\omega = Q_{[p,q,r,s]}^{\omega_L,\omega_P} = \cup_{k \in \mathcal{Z}^+} \widehat{f}\left(\nu_1^k, \nu_2^k, \nu_3^k\right) \tag{20}$$

with $\left(\nu_1^k, \nu_2^k, \nu_3^k\right) \in \left(L_{(p,q)}^{\omega_L} \cap P_{(r,s)}^{\omega_P}\right)$ for the plane-line construction and we take the 1-D inverse discrete Fourier transform of Q on each value of the direction Θ.

The sampling of the extracted Fourier coefficients depends on the 3-D discrete analytical lines used to compute the discrete Radon transform. The 1-D inverse Fourier transform is computed on non-equispaced Fourier coefficients and we need an approximation to the Fourier transform for non-equispaced data or for the computation of the polar Fourier transform [12], [17], [18], [34], [35]. In 2-D, none of these methods were specifically conceived to be invertible and the alternative approaches proposed [21], [26] use an iterative method. In this paper, we want to define a 3-D discrete ridgelet transform that is fast, simple and associated with an exact reconstruction. We consider that the 3-D discrete analytical lines are a good approximation of the Euclidian lines for each line direction and we use a classical discrete Fourier transform defined for equispaced coefficients (for the 2-D case, a similar approach is used in [22] and [23]).

Figure 7 shows projections of an image of size ($55 \times 55 \times 55$) with one white voxel at coordinates $(25, 35, 15)$.

It only represents part of the Discrete Analytical Radon domain composed of 11664 projections. We can see that the 3-D Radon transform follows a broken "line" as in the 2-D transform.
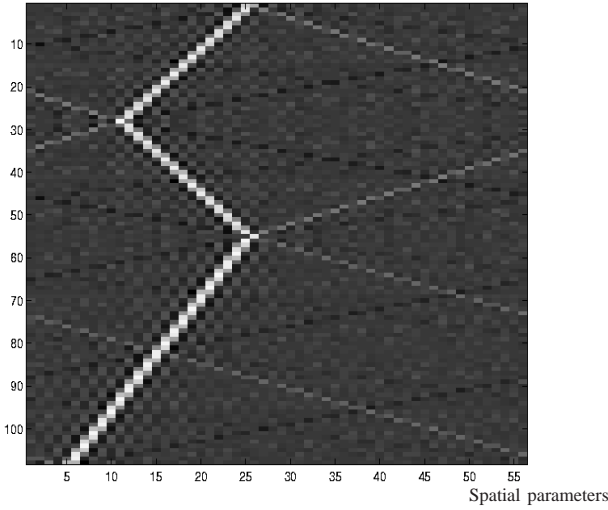
3D Image projections

Fig. 7. Image projections $R_f(.,.,\gamma)$ issued of the 3-D discrete analytical Radon transform function of spatial parameters of an image $I(x,y,z)$.

F. Reconstruction of the 3-D Discrete Radon Transform

Our analytical reconstruction procedure works as follows:

1) Compute the 1-D Fourier transform for each set $R_f(., \Theta, \gamma)$;
2) Substitute the sampled value of $\widehat{f}$ on the lattice where the points fall on 3-D discrete lines with the sampled value of $\widehat{f}$ on the cubic lattice;
3) Apply the 3-D inverse Fourier transform.

Due to the redundancy, some Fourier coefficients belong to more than one discrete line. In this case, the Fourier value is defined by the mean average. The number of times a pixel belongs to a discrete line depends of the frequency (it is more important at low frequencies) and depends of the type of discrete lines.

The 3-D DART followed by its inverse is a one-to-one transform. It provides an exact reconstruction properties if the set of directions of lines provides a complete cover of the cubic lattice:

- With the discrete Radon transform defined with 3-D discrete lines method, the 3-D discrete Radon transform is thus perfectly invertible if the 3-D analytical discrete lines are 3-D supercover lines;
- With the discrete Radon transform defined with discrete planes and 2-D discrete lines, the 3-D Fourier domain is always covered by the analytical 3-D discrete lines for all the presented thickness ($\omega(p,q) \geq \max(|p|, |q|)$). This transform is thus always perfectly revertible.

IV. THE 3-D DISCRETE ANALYTICAL RIDGELET TRANSFORM

A. Definition of the 3-D DART

For the ridgelet transform, we must take a 1-D wavelet transform along the radial variable in Radon space. The choice of a discrete one-dimensional wavelet transform is discussed for the 2-D case by Starck et al. in [22]. The choice of the type of 1-D wavelet transform depends on the goal of the transform. This wavelet transform can be decimated (DWT) or undecimated (UDWT) and the wavelet base can be adapted according to the application, as with the classical wavelet decomposition. In this article, we illustrate the 3-D ridgelet transform with denoising applications. We thus propose to use an undecimated wavelet transform.

Because of decimation after filtering, the Mallat's decomposition is completely time-variant. A way to obtain a time-invariant system is to compute all the integer shifts of the signal. Since the decomposition is not decimated, filters are dilated between each projection. This algorithm presents many advantages, particularly a knowledge of all wavelets' coefficients: coefficients removed during the downsampling are not necessary for a perfect reconstruction, but they may contain useful information for denoising.

B. Redundancy of the 3-D Discrete Analytical Ridgelet Transform

The redundancy factor of 3-D DART representation depends on the 3-D discrete analytical lines used to define the Discrete Radon transform and the type of wavelet transform.

As stated, the thickness parameters allow us to control the redundancy factor of the transform and to adapt it to a given application. Table I shows the different redundancy factor, computed by experimentation, in function of the discrete Radon transform strategies and the object thicknesses.

TABLE I

DISCRETE RADON TRANSFORM REDUNDANCY TABLE.

Discrete objets thicknesses	naive	pythagorician	supercover
3-D discrete planes and 2-D discrete lines	3.9	4.9	9.7
3-D discrete analytical lines	2.6	3.3	6.2

As for the two discrete Radon transform strategies, the voxels covering low frequencies in the Fourier domain belong to more discrete lines than those covering the higher frequency. The redundancy is concentrated mainly in low frequencies.

We can introduce additional redundancy with the wavelet decomposition by using a Undecimated Discrete Wavelet Transform. We increase the factor by the scale number of the UDWT. The redundancy factor of the 3-D DART depends on the wavelet decomposition choice and the scale number (Table II). The most important 3-D DART redundancy factor is obtained with 3-D discrete planes, 2-D discrete lines and an UDWT. For example, this factor is close to 50 with a undecimated wavelet scale 4 decomposition.

TABLE II

DISCRETE RIDGELET TRANSFORM REDUNDANCY TABLE. L IS THE NUMBER OF SCALE

Discrete objets thicknesses	Naive		Pythagorean		Supercover	
Wavelet scale L decomposition	DWT	UDWT	DWT	UDWT	DWT	UDWT
3-D discrete planes and 2-D discrete lines	3.9	$3.9 \times (L+1)$	4.9	$4.9 \times (L+1)$	9.7	$9.7 \times (L+1)$
3-D discrete analytical lines	2.6	$2.6 \times (L+1)$	3.3	$3.3 \times (L+1)$	6.2	$6.2 \times (L+1)$

C. Complexity of the 3-D Discrete Analytical Ridgelet Transform

Let us compute the algorithmic complexity of performing a 3-D Discrete Analytical Ridgelet Transform. We review briefly the algorithm: first, a 3-D discrete Fourier transform is computed on a 3-D image of size $(M \times M \times M)$. 3-D Fourier coefficients are then extracted on each 3-D discrete analytical lines and a 1-D inverse discrete Fourier transform are computed along resulting coefficients to obtain Radon projections. Finally, a wavelet decomposition are computed on each projection.

- The complexity of the 1-D direct/inverse discrete Fourier transform is $\mathcal{O}(n^2)$. The computation of the first step requires $\mathcal{O}(M^6)$ operations.

  In order to cover a 1-D discrete analytical lines we have $\mathcal{O}(M)$ step, because the size of the line is $\frac{M-1}{2}$ and the algorithm of coefficient extraction is linear.

- With the method based on 3-D discrete analytical lines, exposed in paragraph III-C, the 3-D spectra needs $(M-1)(3M-1)$ 3-D supercover lines to be covered. The complexity of this step is $(M-1)(3M-1)\mathcal{O}(M)$, namely $\mathcal{O}(M^3)$.
- With the method based on discrete analytical planes and 2-D discrete analytical lines, exposed in paragraph III-D, the 3-D spectra needs $2M-1$ discrete planes to be covered and each plane of size $n_1 \times n_2$ requires $n_1 + n_2 - 1$ 2-D discrete lines to be covered. The size of a plane is equivalent to $M \times M$. The complexity of this step is thus $(2M-1)^2\mathcal{O}(M)$, namely $\mathcal{O}(M^3)$.
- For each discrete line, we compute a 1-D inverse transform Fourier of complexity $\mathcal{O}(n^2)$. The complexity of this step is thus $(M-1)(3M-1)\mathcal{O}(M^2)$, namely $\mathcal{O}(M^4)$.
  The discrete Radon transform then requires $\mathcal{O}(M^6) + \mathcal{O}(M^3) + \mathcal{O}(M^4) \longrightarrow \mathcal{O}(M^6)$ operations for the first method and $\mathcal{O}(M^6) + \mathcal{O}(M^3) + \mathcal{O}(M^4) \longrightarrow \mathcal{O}(M^6)$ for the second, that is to say $\mathcal{O}(M^6)$ for both of them.
- The complexity of a decimated wavelet decomposition is $\mathcal{O}(n)$. The complexity of this step is thus $(M-1)(3M-1)\mathcal{O}(M)$, namely $\mathcal{O}(M^3)$. Notice that if the wavelet decomposition is undecimated, its complexity is equal to $\mathcal{O}(n \log n)$.
  The 3-D discrete analytical ridgelet transform therefore gives a total of $\mathcal{O}(M^6)$ operations. If $N = M \times M \times M$ is the number of samples of the video then the complexity our algorithm is $\mathcal{O}(N^2)$.

The computation of the 3-D DART can also use the fast Fourier transform of complexity $\mathcal{O}(n \log n)$. Consequently, the total complexity becomes $\mathcal{O}(M^6 \log M)$ or $\mathcal{O}(N^2 \log N)$ with N the number of samples. We can remark that the complexity of our algorithm depends on the complexity of the Fourier transform.

Algorithms have been developped with ©Matlab software on a AMD Athlon™ 64 2800+ single processor and a GNU/Linux system. The 3-D DART, using naive planes, 2-D naive discrete lines and an undecimated wavelet scale 4 decomposition, is computed in 32 seconds for a 3-D image of size $(63 \times 63 \times 63)$ and uses 33.4 Mega-octets with 64-bit data. It is computed in 342 seconds for a 3-D image of size $(127 \times 127 \times 127)$ and uses 276 Mega-octets with 64-bit data.

D. Definition of the 3-D Local-DART

The ridgelet transform can be easily extended to a local transform by a smooth partitioning: in 2-D, the image is smoothly windowed into squares and we analyse each square by the ridgelet transform. The local ridgelet transform is used to introduce redundancy in 2-D image restorations and to process locally 2-D image contours. For this decomposition, the analysis is better localized in the spatial domain. This property eliminates the parasitic lines present in the ridgelet reconstruction due to the selection of an important contour in an area of the image [22].

The 3-D DART can be easily extended to a local transform by the smooth partitioning windowed into cubes. Each cube is analysed by the DART.

To define the smooth partitioning, we have adapted the method detailed in [22] to our discrete transform. In 1-D, the interpolation of a point value $f(i)$ from its two 1-D block values $B_1(i_1)$, $B_2(i_2)$ of size $l = \frac{b+1}{2}$ with $i_1 \geq l$ and $i_2 = i_1 - l + 1$ (figure 8) is defined by:

$$f(i) = \Omega\left(\frac{i_2}{l}\right) B_1(i_1) + \Omega\left(1 - \frac{i_2}{l}\right) B_2(i_2) \tag{21}$$

with $\Omega(x) = \cos^2\left(\frac{\pi x}{2}\right)$ and respect the symmetry property $\Omega(x) + \Omega(1-x) = 1$.
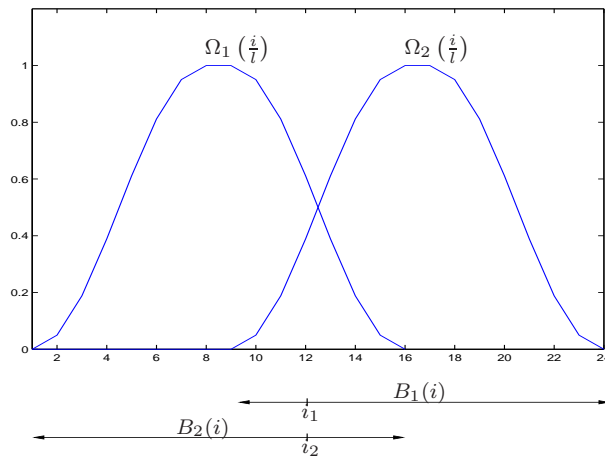

Fig. 8.   1-D smooth windowing.

The 3-D voxel calculation is the simple extension of the 1-D formulation in the 3-D space.

We calculate a voxel value $f(i, j, k)$ from its eight 3-D block values of size $l \times l \times l$ with $l = \frac{b+1}{2}$: $B_1(i_1, j_1, k_1)$, $B_2(i_1, j_1, k_2)$, $B_3(i_1, j_2, k_1)$, $B_4(i_1, j_2, k_2)$, $B_5(i_2, j_1, k_1)$, $B_6(i_2, j_1, k_2)$, $B_7(i_2, j_2, k_1)$, $B_8(i_2, j_2, k_2)$ with $i_1, j_1, k_1 \geq l$ and $i_2 = i_1 - l + 1$, $j_2 = j_1 - l + 1$, $k_2 = k_1 - l + 1$ such as:

$$f_k^{a,b} = \Omega\left(\frac{k_2}{l}\right) B_a(i_1, j_1, k_1) \tag{22}$$

$$+ \Omega\left(1 - \frac{k_2}{l}\right) B_b(i_1, j_1, k_2) \tag{23}$$

where a and b are the block numbers $((a, b) = (2n + 1, 2n + 2)_{n=0\ldots3})$ and:

$$f_{j,1} = \Omega\left(\frac{j_2}{l}\right) f_k^{1,2} + \Omega\left(1 - \frac{j_2}{l}\right) f_k^{3,4} \tag{24}$$

$$f_{j,2} = \Omega\left(\frac{j_2}{l}\right) f_k^{5,6} + \Omega\left(1 - \frac{j_2}{l}\right) f_k^{7,8} \tag{25}$$

$$f(i, j, k) = \Omega\left(\frac{i_2}{l}\right) f_{j,1} + \Omega\left(1 - \frac{i_2}{l}\right) f_{j,2} \tag{26}$$

The local-DART also introduces redundancy. This 3-D partitioning with cubic block increases the redundancy:

$$\rho = \left(\frac{l * n}{L}\right)^3 = \left(\frac{2L - l + 1}{L + \frac{L}{l}}\right)^3 \tag{27}$$

where L is the 3-D image size, l the block size and n the block number.

V. DENOISING APPLICATIONS

A. Principles

In order to illustrate the 3-D DART potentiality, we present synthetic image and video denoising with a classic denoising process.

The denoising procedure by ridgelet transform simply consists in thresholding the ridgelet coefficients and computing the inverse ridgelet transform. The thresholding is performed with the help of an undecimated method (UDWT) developed for the Daubechies D8 wavelet scale 4 decomposition [36]. Let r_f be the noisy undecimated ridgelet coefficients, we use the following hard-thresholding:

$$r_f(a, b, \Theta) = \begin{cases} r_f(a, b, \Theta) & \text{if } |r_f(a, b, \Theta)| \geq \alpha\sigma \\ 0 & \text{otherwise} \end{cases} \tag{28}$$

α can be defined as $\alpha = \sqrt{2 \log(N)}$ or as $\alpha = 3$, and the variance σ is estimated using the absolute median of the wavelet decomposition's first scale of each radial projection [37].

In order to study precisely the result of the denoising algorithm with different types of discrete analytical lines we have generated an artificial 3-D object and added important white noise. With a more redundant decomposition (based on supercover discrete lines and planes) the denoising result is better than for a less redundant decomposition (naive 2-D lines and planes): in general the edge is reconstructed more precisely and the uniform areas are smoother. As in the wavelet decomposition, overcompletness provides advantages for denoising. Table III illustrates this phenomena: we present the mean SNR of five denoised videos with the three types of discrete analytical lines. We remarks that the more important thickness is, better the quality of denoising is in term of SNR that confirms the visual constatation.

TABLE III

MEAN SIGNAL TO NOISE RATES FOR DENOISINGS WITH DART DEFINED WITH DIFFERENT DISCRETE ANALYTICAL OBJECT THICKNESS (IN dB).

	Noise	Naive	Pythagorean	Supercover
SNR	6.34	10.84	10.90	11.35

In order to obtain the 3-D images and videos denoising results presented in this paper, we propose to use the discrete Radon transform defined with naive planes and 2-D discrete naive lines. This choice indeed corresponds to the faster algorithm of our proposed methods. Moreover, it corresponds to the less redundant reconstructible decomposition and is associated to inferior performance since the overcompletness provides advantages for denoising.

We compare the denoising of different 3-D images by thresholding of the 3-D DART and of the 3-D undecimated wavelet decomposition. We use the Signal to Noise Rate[4] (SNR) and the visual analysis to measure the performance.

---

[4] The SNR computation is extracted from Vetterli and Kovacenic 's book [38]. It is available in the Minh Do's FRIT ©Matlab Toolbox, http://www.ifp.uiuc.edu/~minhdo/software/frit_toolbox.tar.gz

B. Denoising of a synthetic image

The image is a synthetic cube of size $(63 \times 63 \times 63)$ with 256 levels of grey (figures 9a). A white Gaussian noise is added to this 3-D image[5] (figure 9b) with as the Signal to Noise Ratio equal to 9.62 dB.

The SNR of the 3-D image denoised by the 3-D DART strategy (18.25 dB) is higher than that of the 3-D image denoised by an undecimated wavelet decomposition (13.45 dB). We can see (figures 9(c) and 9(d)) that the edge is more precisely reconstructed and that the uniform areas are smoother for the DART than for the UDWT.

(a)   (b)
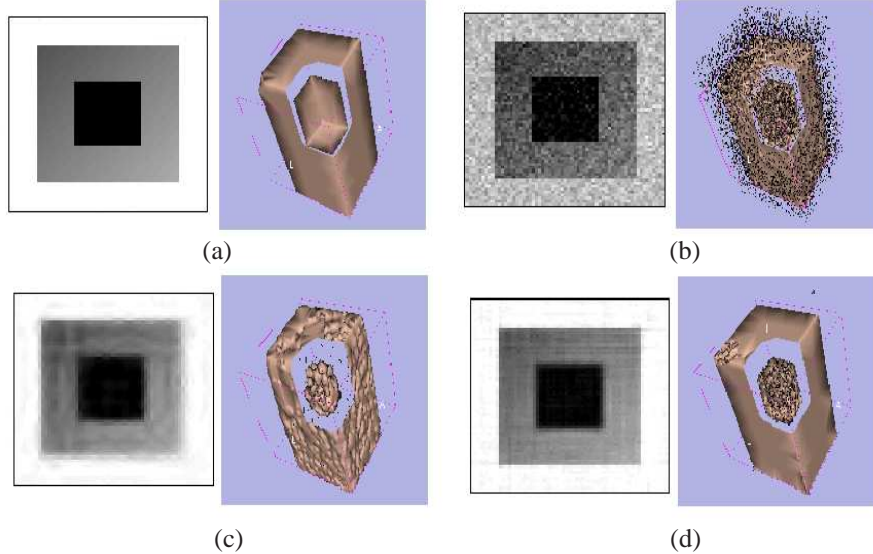
(c)   (d)

Fig. 9.   Slices and 3-D views: (a) original image, (b) noisy image, (c) denoised image with 3-D wavelet transform and (d) denoised image with a 3-D DART.

VI. COLOUR VIDEO DENOISING

A. Principle

Carré and Andres have studied colour image denoising with the 2-D DART [39], [40]. We propose to extend our 3-D DART strategies0 to colour video denoising using the 3-D local DART. For this, we consider the video as a spatio-temporal volume and we apply the same denoising processing by the 3-D DART as the previous 3-D image denoising [41].

The video is a sequence of 279 images of size (279×279) with their three-colour components (figure 12 (a)). It comes from the Video Quality Experts Group[6] (V.Q.E.G.) .

A Gaussian noise is added to the three-colour components of the video. The colour video is decomposed into three videos corresponding to the three-colour components. We independently denoise every component with the associated 3-D local Discrete Analytical Ridgelet Transform and we reconstruct the video with the inverse 3-D local-DART. The local denoising processing is applied to blocks of size $(71 \times 71 \times 71)$.

Setting the size of the blocks is a difficult problem. The more 3-D blocks, the more the 3-D DART redundancy increases (and thus the better the denoising results are). However the size of block must not be too small to compute a wavelet decomposition on each projection with a satisfactory number of level and to conserve an algebraic exactness, a geometric fidelity. It is the same problem for all the windowed or local transforms (as spectrogram, Malvar Wavelet ...).

B. Comparison with other 3-D transforms

First, the 3-D DART is compared to two reference transforms with a noisy video ($\sigma = 42$) in RGB colour representation (figure 10(b)):

- a 3-D undecimated Daubechies D8 wavelet scale 4 transform [42], [43],
- a 3-D dual tree complex wavelet scale 4 transform [27].

Denoising results are evaluated with a soft thresholding scheme as proposed in [27] and the same threshold is used for each subband of the three type of transforms (figure 10).

[5]3-D views constructed with 3-D Slicer: http://www.slicer.org/
[6]http://www.its.bldrdoc.gov/vqeg/index.php

TABLE IV

Signal to Noise Rates applied on each denoised color component of a frame (in dB).

	Noisy		3-D UDWT	
	SNR_1	SNR_2	SNR_1	SNR_2
Red	5.88	27.42	10.84	32.09
Green	5.97	26.05	11.32	30.63
Blue	5.07	20.64	10.42	25.30

	3-D dual tree transform		3-D DART	
	SNR_1	SNR_2	SNR_1	SNR_2
Red	11.69	31.81	12.44	32.44
Green	12.17	30.39	13.09	31.18
Blue	11.78	25.54	13.22	26.70

(a) Extract from the original video

(b) Extract from the noisy video

(c) Extract from the video denoised with a 3-D undecimated wavelet transform

(d) Extract from the video denoised with a 3-D dual tree complex wavelet transform

(e) Extract from the video denoised with the 3-D naive DART

Fig. 10. Images extracted from noisy and denoised videos

Denoising result with the 3-D dual tree complex wavelet (figure 10(d)) is perceptually better than with the 3-D undecimated wavelet decomposition (figure 10(c)). Artefacts are present in both 3-D transforms due to wavelet coefficient with important information thresholding. These artefacts are not present in the denoising result with the 3-D DART (figure 10(e)).

In order to make a more complete comparison, we study the SNR means computed after the denoising of five color videos. Moreover, we use two numerical definitions for the SNR measure: the first SNR computation, noted SNR_1, is extracted from Vetterli and Kovacenic's book [38] and the second SNR computation, noted SNR_2, is a part of *WaveLab*[7]. Table IV illustrates these measures.

The SNR calculations show that the 3-D DART is better than the 3-D undecimated wavelet transform and the 3-D dual tree complex wavelet transform. This simple experimentation illustrates the fact that the 3-D DART is competitive for video denoising.

C. Color denoising

We have studied the colour video denoising with the DART in several classical colour spaces :

- Red, Green and Blue : the most used in colour image processing because of material dependance,
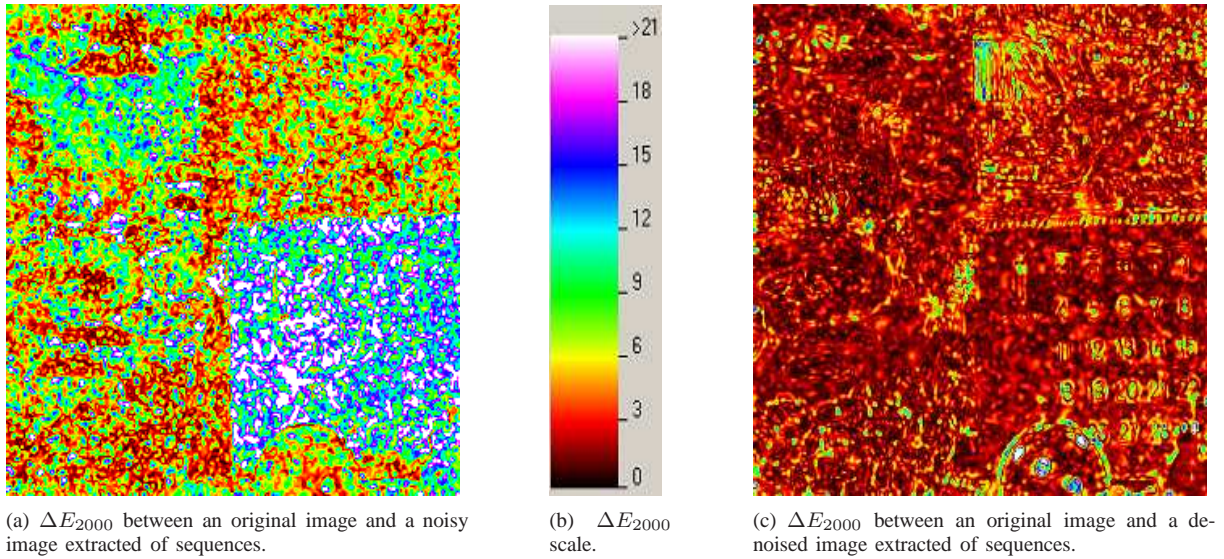
[7]Wavelab is a ©Matlab toolbox available in http://www-stat.stanford.edu/~wavelab/

(a) ΔE_{2000} between an original image and a noisy image extracted of sequences.

(b) ΔE_{2000} scale.

(c) ΔE_{2000} between an original image and a denoised image extracted of sequences.

Fig. 11.   S-CIELAB ΔE_{2000} calculations.

- Hue, Saturation and Value : colour representation with separated components more subjective,
- Y (luminance), Cb (blue chrominance) and Cr (red chrominance) : international standard dedicated image digital coding,
- XYZ : correct some RGB defaults, the Y component is considered as the luminance of the incident spectra,
- Principle Components Analysis : projection of the voxel colour on the factoriel axis.

First studies have showed that RGB and YCbCr spaces are the good colour representation for video denoising with the 3-D DART. Similar conclusions are obtained in the 2-D case.

We illustrate two examples of denoising:

- Restoration of the less noisy video $\sigma = 42$ in RGB colour representation (figure 12).
- Restoration of the very noisy video $\sigma = 264$ in YcrCb colour representation (figure 13).

First, we can see in figure 12 that the quality of colours and linear forms perception are very encouraging for the colour video denoising: colours in the video after the denoising are not debased. The rectilinear contours, those of the train or the green hedge for example, are maintained and not destorted. Futhermore, we correctly restore zones containing small objects, for example the numbers on the calendar. The 3-D DART allows to process the temporal evolution like contours.

Now, we propose to evaluate the robustness of our method with very noisy data (figure 13(a): $\sigma = 264$). The denoising results (figure 13(b)) are correct with regard to the noisy video: colours and contours of the different animals are correctly restored. But with this level of noise, the calendar numbers are difficult to read.

In order to evaluate the preserving of the original colour during the denoising process, we propose to use a perceptual colour measure. We have compared results using the S-CIELAB [44] ΔE_{2000} calculations [45]–[47], a perceptual colour fidelity metric. A high ΔE_{2000} between an original image and a processed image corresponds to an important colorimetric difference.

We have extracted a noisy image of less noisy video (figure 12) and the corresponding denoised image by local-DART to measure how accurate the reproduction of a colour is compared to one the original when viewed by a human observer. The presented measures are calculated for an observer visualizing images at 47 cm away from a monitor displaying 72 dots per inch.

In figure 11(a), the ΔE_{2000} between the original and the noisy image shows an important perceptual colour difference mainly on colours close to white and on detailed zones like the calendar.

The ΔE_{2000} is better on denoised homogeneous coloured zones (figure 11(c)) likewise on colours close to white. The calendar is more perceptually correctly restored. However the restored calendar numbers are of low perceptual quality.

The house roof on the calendar, composed of straights, is not correctly restored. The rectilinear forms correspond to some discrete analytical ridgelet coefficients a part of which has been thresholded.

These perceptual colour difference results show that we improve the human observer perception of videos denoised with the 3-D DART.

VII. CONCLUSION

So far, the development of the 2-D discrete ridgelet transform has been investigated by three teams in previous works. In this paper, we have proposed an implementation of the 3-D ridgelet transform. Our innovative choice is to extend the ridgelet

transform to 3-D by using the formalism of the discrete analytical geometry theory in the Fourier domain. We thus define a 3-D discrete ridgelet transform: the 3-D Discrete Analytical Ridgelet Transform (3-D DART). In this paper, we have proposed two strategies to implement the 3-D Discrete Analytical Ridgelet Transform: 3-D discrete radial lines going through the origin defined from their orthogonal projections and 3-D planes covered with 2-D line segments. The two 3-D DART algorithms are easy to implement. It provides an exact reconstruction property: the 3-D DART followed by a reverse 3-D DART is a one-to-one transform. Our experiments have shown that our approach is based on a geometrically faithful notion of ridgelets: the associated 3-D discrete Radon decomposition of an array containing a single nonzero entry follows a broken line. Moreover, by using the analytical formalisation, we define a flexible ridgelet transform: we can define different 3-D DART decompositions according to the arithmetical thickness of the analytical discrete lines.

We have illustrated the performances of the DART for denoising problems with Gaussian noise. This study indicates that the DART and the Local-DART thresholding are outstanding in the 3-D image denoising and enable an effective denoising of a colour video, even with very noisy videos.

This work can be extended to several directions. One of the theoretical questions in discrete geometry is the problem of defining an arithmetical thickness 3-D function that provides a smaller redundancy and a cover of the Fourier cube. This is still an open and difficult arithmetical problem. One of the most important interests of the discrete analytical approach is the possibility to easily extend our work to n-D (we are investigating the application of a 4-D DART to the denoising process of animated 3-D images). We propose to extract the Fourier coefficients along a n-D discrete analytical line going through the origin. The principle of the n-D method is the same as in the 3-D case with the same properties (exact reconstruction, rapidity, flexible definition). The choice of colour basis for the denoising problematic remains an opened problem through.

APPENDIX I
2-D DISCRETE FOURIER SPECTRA COVERING WITH 2-D DISCRETE ANALYTICAL LINES

Proposition 2 :
Let a square lattice be defined as $\Omega_N^2 = [-N, N] \times [-M, M]$. Let us consider the set of directions (p_m, q_m) with, for $0 \leq m \leq 2N$, $(p_m, q_m) = (N, m - N)$ and for $2N + 1 \leq m \leq 4N - 2$, $(p_m, q_m) = (m - 3N + 1, N)$. The set of all the closed lines defined by $|p_m f_1 + q_m f_2| \leq \omega_m / 2$ with $\omega_m \geq \sup(|p_m|, |q_m|)$ provides a complete cover of the lattice Ω_N^2.

Proof :
The proof of this proposition is obvious because of a well known result in discrete analytical geometry that states that a closed discrete line of direction (p, q) is connected if and only if $\omega \geq \sup(|p|, |q|)$ [30]. For thinner (non connected) discrete lines, with values of $\omega < \sup(|p|, |q|)$, it is possible but not certain that we also achieve a complete cover of the lattice Ω_N^2 depending on the value of ω compared to N. However, for our applications, we preferred working with connected discrete lines.

REFERENCES

[1] E. Candès, "Ridgelets : Theory and applications," Ph.D. dissertation, University of Stanford, August 1998.
[2] M. Do, "Directional multiresolution image representations," Ph.D. dissertation, Department of Communication Systems, Swiss Federal Institute of Technology Lausanne, November 2001.
[3] A. Flesia, H. Hel-Or, A. Averbuch, E. Candès, R. Coifman, and D. Donoho, "Digital implementation of ridgelet packets," in *Beyond Wavelets*, J. Stoeckler and G. V. Welland, Eds. Academic Press, 2002.
[4] P. Carré and E. Andrès, "Discrete Analytical Ridgelet Transform," *Signal Processing*, vol. 84, no. 11, November 2004.
[5] P. Querre, J. L. Starck, and V. Martinez, "Analysis of the galaxy distribution using multiscale methods," in *Astronomical Data Analysis Conference*, J. Starck and Murtagh, Eds., vol. 4847. SPIE Conference, 2002.
[6] J.-L. Starck, V. Martinez, D. Donoho, O. Levi, P. Querre, and E. Saar, "Analysis of the spatial distribution of galaxies by multiscale methods," *Eurasip Journal on Applied Signal Processing, special issues on applications of signal processing in Astrophysics and Cosmology*, vol. 5, pp. 2455–2469, 2005.
[7] D. Donoho and O. Levy, "Fast X-ray and beamlet transforms for three-dimensional data," in *Modern Signal Processing*, C. U. Press, Ed. MSRI Publications, 2002, vol. 46, pp. 79–116.
[8] A. Averbuch and Y. Shkolnisky, "3D Fourier based discrete Radon transform," *Applied and Computational Harmonic*, vol. 15, pp. 33–69, 2003.
[9] S. Mallat, "A theory for multiresolution signal decomposition : the wavelet transform," *IEEE Trans. on PAMI*, vol. 11, no. 7, pp. 674–693, 1989.
[10] F. Matus and J. Flusser, "Image representation via a finite Radon transform," *IEEE Trans. on Pattern Analysis and Machine Intelligence*, vol. 15, no. 10, pp. 996–1006, 1993.
[11] F. Natterer, *The Mathematics of Computerized Tomography*. Wiley, 1986.
[12] P. Toft, "The Radon transform, theory and implementation," Ph.D. dissertation, Department of Mathematical Modelling, Section for Digital Signal Processing, Technical University of Denmark, 1996.
[13] J. Roerdink and M. Westenberg, "Data-parallel tomographic reconstruction: a comparison of filtered backprojection and direct Fourier reconstruction," *Parallel Computing*, vol. 24, pp. 2129–2144, 1998.
[14] M. Brady, "A fast discrete approximation algorithm for the Radon transform," *SIAM J. Computer*, vol. 27, no. 1, pp. 107–119, February 1998.
[15] D. Potts and G. Steidl, "A new linogram algorithm for computerized tomography," *IMA Journal of Numerical Analysis*, vol. 21, pp. 769–782, 2001.
[16] J. Fessler and B. Sutton, "Nonuniform fast Fourier transforms using min-max interpolation," *IEEE Transactions on Signal Processing*, vol. 51, no. 2, p. 560574, February 2003.
[17] K. Fourmont, "Non-equispaced fast fourier transforms with applications to tomography," *Journal of Fourier Analysis and Applications*, vol. 9, no. 5, pp. 431–450, September 2003.
[18] M. Bronstein, A. Bronstein, M. Zibulevsky, and H. Azhari, "Reconstruction in diffraction ultrasound tomography using non-uniform FFT," *IEEE Trans. Med. Imaging*, vol. 21, no. 11, pp. 1395–1401, 2002.
[19] M. Do and M. Vetterli, "Image denoising using orthonormal finite ridgelet transform," in *SPIE Conference on Wavelet Applications in Signal and Image Processing VIII*, San Diego, USA, august 2000.

(a) (b) (c)

Fig. 12. Extracting of four images issued: (a) original colour video, (b) noisy colour video and (c) colour video denoised with the 3-D DART in RGB space.

[20] ——, "The finite ridgelet transforms for image representation," *IEEE Transactions on Image Processing*, vol. 12, pp. 16–28, January 2003.

[21] A. Averbuch, R. Coifman, D. Donoho, M. Israeli, and J. Walden, "Fast slant stack: A notion of Radon transform for data in a cartesian grid which is rapidly computible, algebraically exact, geometrically faithful and invertible," *SIAM Scientific Computing*, vol. to appear, 2001.

[22] J.-L. Starck, E. Candès, and D. Donoho, "The curvelet transform for image denoising," *IEEE Transactions on Image Processing*, vol. 11, no. 6, pp. 670–684, November 2002.

[23] P. Carré and E. Andres, "Ridgelet transform based on Réveillès discrete lines," in *DGCI*, April 2002.

[24] D. Helbert, P. Carré, and E. Andres, "La transformée ridgelet analytique discrète 3D," in *GRETSI*, Paris, France, septembre 2003.

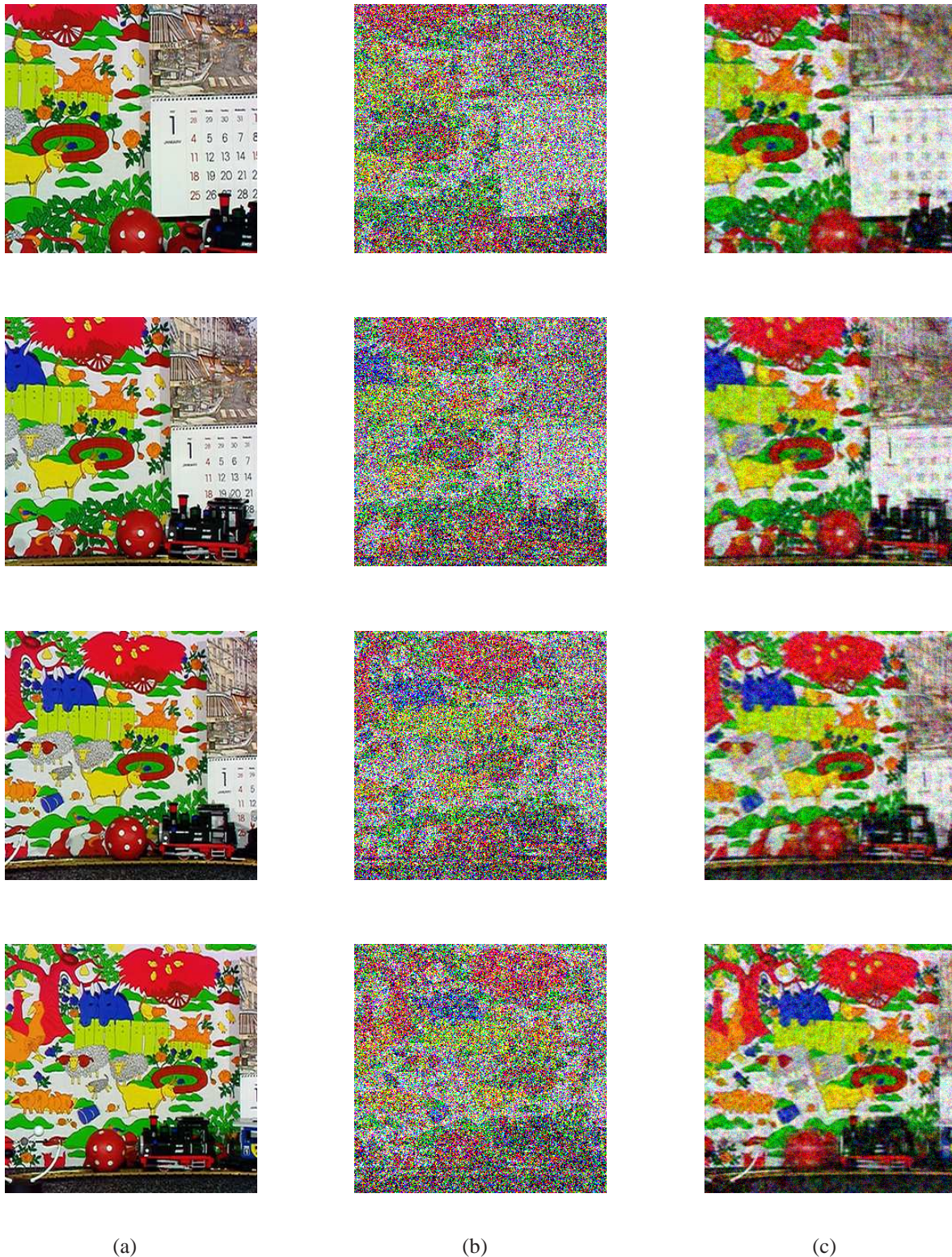(a)   (b)   (c)

Fig. 13.   Extracting of four images issued: (a) original colour video, (b) noisy colour video and (c) colour video denoised with the 3-D DART in YCrCb space.

[25] P. Carré, D. Helbert, and E. Andres, "3-D fast ridgelet transform," in *IEEE International Conference on Image Processing*, vol. 1, Barcelona, Spain, september 2003, pp. 1021–1024.

[26] A. Averbuch and Y. Shkolnisky, "3D discrete x-ray transform," *Applied and Computational Harmonic Analysis*, vol. 17, pp. 259–276, 2004.

[27] I. Selesnick and K. Li, "Video denoising using 2d and 3d dual-tree complex wavelet transforms," in *Wavelet Applications in Signal and Image Processing X*, SPIE, Ed., vol. 5207, San Diego, August 2003.

[28] L. Ying, L. Demanet, and E. Candes, "3d discrete curvelet transform," in *Wavelets XI conference*, SPIE, Ed., San Diego, july 2005.

[29] Y. Lu and M. Do, "3-d directional filter banks and surfacelets," in *Conference on Wavelet Applications in Signal and Image Processing XI*. San Diego: SPIE, August 2005.

[30] J. Réveillès, "Géométrie discrète, calcul en nombres entiers et algorithmique," Strasbourg, France, 1991.

[31] E. Andres, "Discrete linear objects in dimension n: The standard model," *Graphical Models*, no. 65, pp. 92–111, 2003.

[32] D. Wagner, M. Tajine, and C. Ronse, "An approach to discretization based on the Hausdorff metric," in *International Symposium on Mathematical Morphology*. Kluwer Academic Publishers, 1998, pp. 67–74.

[33] E. Andres, R. Acharya, and C. Sibata, "Discrete analytical hyperplanes," *CVGIP: Graphical Model and Image Processing*, vol. 59, no. 5, pp. 302–309, 1997.

[34] F. Natterer, "Numerical methods in tomography," *Acta Numerica*, 1999.

[35] D. Potts, G. Steidl, and M. Tasche, "Fast Fourier transforms for nonequispaced data: a tutorial," in *J.J. Benedetto, P.J.S.G. Ferreira (Eds.), Modern Sampling Theory: Mathematics ans Applications*, 2001, pp. 247–270.

[36] I. Daubechies, "Orthonormal bases of compactly supported wavelets," *Commun. on Pure and appl. Math.*, vol. 41, pp. 909–906, November 1988.

[37] D. Donoho, "Wavelet shrinkage and W.V.D. : a 10-minute tour," Stanford University, Tech. Rep., 1992.

[38] M. Vetterli and J. Kovacević, *Wavelets and Subband Coding*, ser. Signal Processing. New Jersey: Prentice Hall PTR, 1995.

[39] P. Carré and E. Andres, "Discrete ridgelet transform : application to the denoising of color images," in *CGIV*, Poitiers, France, April 2002.

[40] D. Helbert, P. Carré, and E. Andres, "Color image restoration on the 2-D discrete analytical ridgelet transform," in *IST Beijing International Conference on Imaging*, Beijing, China, May 2005.

[41] P. Carré and D. Helbert, "Ridgelet decomposition: discrete implementation and color denoising," in *Wavelet Applications in Industrial Processing III*. Boston, Massachusetts, USA: SPIE, October 2005, invited paper.

[42] S. Mallat and S. Zhong, "Characterization of signals from multiscale edges," *IEEE Trans. on PAMI*, vol. 14, no. 7, pp. 710–732, July 1992.

[43] M. Shensa, "Wedding the à trous and Mallat algorithms," *IEEE Trans. Signal Processing*, vol. 40, no. 10, pp. 2464–2482, 1992.

[44] Zhang and Wandell, "A spatial extension of CIELAB for digital color image reproduction," in *SID Journal*, 1997.

[45] M. Luo, G. Cui, and B. Rigg, "The development of the CIE 2000 colour difference formula: CIEDE 2000," *Color Research and Application*, vol. 26, pp. 340–350, october 2001.

[46] Commission Internationale de l'Eclairage, *Improvement to industrial colour-difference evaluation*. Central Bureau of CIE, Vienna, Austria: CIE Publication, 2001.

[47] M. Luo, G. Cui, and B. Rigg, "Further comments on CIEDE 2000," *Color Research and Application*, vol. 27, pp. 127–128, april 2002.

David Helbert received his Master degree in Information Processing in 2002 and his Ph.D. degree in Signal and Image Processing and Computer Science at the University of Poitiers, France, for his works on the image restoration and the information fusion in 2005. He is Associate Professor at the University of Poitiers in the Electronic department and member of the Signal, Image and Communication laboratory. His main research interests are in image processing, multiresolution analysis, discrete geometry, information fusion and 3D reconstruction in various field such as image restoration, multispectral image analysis, object tracking and 3D animation.

Philippe Carré received the Engineer degree in Computer Engineering from Compiegne University of Technology, France, in 1995, and the Ph.D. degree in Signal Processing and Computer Science in University of Poitiers, France, in 2000 for his work on the definition of discrete atomic Time-Frequency representations. He is presently Associate Professor at University of Poitiers in the Electronic department and member of the Signal, Image and Communication laboratory. His interests include signal and image processing, wavelets, Time-Frequency and multiscale decompositions theory and their applications to the fields of denoising, segmentation and watermarking.

Éric Andres obtained his Master degree in Computer Science in 1989, and his Ph.D in Computer science on discrete rotations in 1992 at the University of Strasbourg (France). After 2 years in Buffalo (NY) at the Roswell Park Cancer Institute, he got a position as Assistant Professor at the University of Poitiers in 1997. Since 2001, he is professor in Computer Science at this same university. Éric Andres is specialized in discrete analytical geometry. He works on describing analytically discrete objects and operations, reconstruction operations and the relationship between discrete and continuous geometry. For a couple of years now, he is developing a discrete modelling software that allows to manipulate discrete and continuous embeddings of geometrical objects.